Made available through Montana State University's ScholarWorks

Model of Disk-Averaged Moon Polarization

Erica Venkatesulu; Riley D. Logan; Joseph A. Shaw

Accessibility Disclaimer:

For a more accessible version of this document, please submit an accessibility request form through the Montana State University Library website.

Model of Disk-Averaged Moon Polarization

Erica Venkatesulu, Riley D. Logan, *Member, IEEE*, and Joseph A. Shaw, *Senior Member, IEEE*

***Abstract*—The Moon can be used as a stable calibration target for on-orbit satellite instruments without the need for solar diffusers or atmospheric correction. Radiometric models of the Moon have been developed to enable lunar calibration; however, to the authors' knowledge, a polarization model of the Moon to improve lunar calibration of polarization-sensitive instruments has not been published. In this work, models of the disk-averaged degree of linear polarization (DoLP) in terms of lunar geometry variables were developed for nine spectral bands (336, 365, 383, 450, 519, 650, 800, 900 nm, and a broadband channel with a response from 400 to 1000 nm) using measurements from three previously published datasets. The set of models was named the Lunar disk-Averaged Model of Polarization (LAMP). LAMP includes two types of models: a model dependent on phase angle and Sun selenographic longitude was used for all nine channels, and a second model incorporating libration variables (observer selenographic latitude and longitude) was used for the three channels with the most observations. The majority of the residuals for the simpler model of DoLP were within 0.01, and the majority for the model with libration dependence were within 0.005 (for measured DoLP values ranging from −0.016 to 0.204).**

***Index Terms*—Calibration, moon, optical polarization, polarimetry, radiometry.**

I. Introduction

EARTH-OBSERVING satellites contribute critical measurements to applications ranging from monitoring Earth's radiation budget [1], [2] to estimating evapotranspiration for better understanding of the water cycle [3] to predicting the spread of malaria [4]. The quality of data from these satellites depends directly on the calibration of the onboard instruments [5], [6]. It is also important to be able to compare measurements from different satellite instruments for maintaining long-term records [2] or obtaining more frequent measurements of a particular location on Earth.

There are a variety of methods to perform calibration and intercomparison of satellite instruments. Solar calibration can be performed using a solar diffuser to track changes in the response of the reflective solar bands of the instrument [7], [8], [9], [10], [11]; however, due to degradation of solar diffusers, it is common to use solar diffuser stability monitors [9], [10] or multiple solar diffusers at different temporal intervals [11]. Some satellites include calibration sources such as lamps [12] or blackbodies [13] to monitor the performance of detectors operating in different spectral ranges, but the stability of these sources over time must also be monitored. Other calibration targets include pseudo-invariant calibration sites (PICS) [14] and instrumented sites [15], [16], [17] on Earth's surface and deep convective clouds [18], which can be used for long-term trending, intercalibration, and even absolute radiometric calibration. Also, in the future, SI-traceable satellites will be available on orbit for cross calibration of other satellite instruments [19]. However, these methods require some atmospheric correction to infer the signal from the calibration target, inducing additional uncertainties. The Moon has increasingly been used as a target for on-orbit calibration, avoiding some of the challenges associated with other calibration methods. The surface of the Moon is extremely stable and a similar reflectance to Earth scenes, so lunar calibration does not require a diffuser for use as a calibration target and is not limited in accuracy by the performance of a stability monitor. The Moon is outside the atmosphere, so lunar calibration is also not limited in accuracy by the performance of an atmospheric correction.

Multiple studies measured or plan to measure and model the unpolarized spectral irradiance of the Moon to enable and improve lunar calibration [20], [21], [22], [23], [24]. In particular, the model based on measurements from the RObotic Lunar Observatory (ROLO) has been widely used [20]. Largely enabled by ROLO, the Moon has since been used as a reference for on-orbit calibrations [25], [26], [27], [28], [29], [30] and intercomparisons [31] of many satellite instruments. However, for polarimeters or other instruments with polarization sensitivity, the polarization of the Moon would create errors in lunar calibration if these previously published unpolarized measurements and models were used without accounting for polarization.

The literature has recognized the relative lack of work in measuring and modeling Moon polarization, and the potential benefit of such work [32]. This article introduces a Lunar disk-Averaged Model of Polarization (LAMP) that predicts the disk-averaged degree of linear polarization (DoLP) as a function of lunar geometry variables based on DoLP measurements across nine spectral channels ranging from 336 to 900 nm. Modeling the disk-averaged DoLP is useful for supplementing the models of disk-averaged lunar radiance that are currently used in lunar calibrations (where all the pixels imaging the Moon are averaged). A very preliminary version of the model described in this article was presented in the conference proceedings of Polarization Science and Remote Sensing XII

Received 8 July 2025; revised 30 October 2025; accepted 29 November 2025. Date of publication 4 December 2025; date of current version 26 December 2025. This work was supported in part by the National Science Foundation Graduate Research Fellowship Program under Grant 2439625; in part by the National Science Foundation Established Program to Stimulate Competitive Research (EPSCoR) Cooperative under Agreement OIA-2242802; and in part by the Optical Technology Center and Office of the Vice-President of Research and Economic Development, Montana State University. An earlier version of this paper was presented at the Polarization Science and Remote Sensing XII Conference, SPIE Optics and Photonics, 2025 [DOI: 10.1117/12.3063663]. *(Corresponding author: Joseph A. Shaw.)*

The authors are with the Optical Technology Center and the Electrical and Computer Engineering Department, Montana State University, Bozeman, MT 59717 USA (e-mail: joseph.shaw@montana.edu).

Digital Object Identifier 10.1109/TGRS.2025.3640557

© 2025 The Authors. This work is licensed under a Creative Commons Attribution 4.0 License.
For more information, see https://creativecommons.org/licenses/by/4.0/

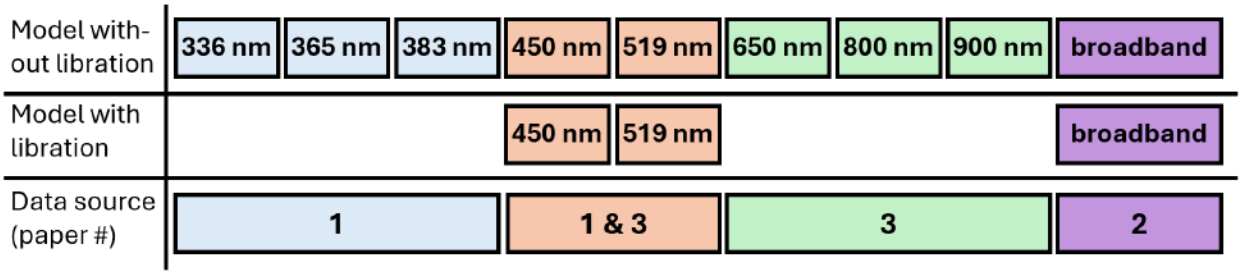


Fig. 1. Summary of the source of data for each of the nine channels: Paper 1 refers to data from Coyne and Pellicori [34], Paper 2 refers to data from Venkatesulu and Shaw [35], and Paper 3 refers to data from Venkatesulu et al. [37]. The figure also describes which channels were fit to models with and without libration variables.

[33]; the model presented here has been expanded to include libration variables and data from other authors available in the literature. The remainder of this article describes how the datasets were combined, explains the model and when libration was used, presents the resulting fits with example plots, shows example predictions of DoLP, and compares LAMP to a preliminary model of DoLP recently added to the previously published Lunar Irradiance Model of the European Space Agency (LIME) [24].

II. Dataset

We combined data from Coyne and Pellicori [34] with data that we previously recorded (broadband data published [35] and publicly available [36]; data in visible and near infrared (VNIR) spectral bands published [37] and publicly available [38]). We recorded high-spatial-resolution images in those studies, which could theoretically contribute to a disk-resolved model of the Moon, but our objective for this model was to predict the disk-averaged DoLP. This section describes our methods for manipulating those data to form the combined dataset that is the basis of the lunar polarization model.

The data from Coyne and Pellicori [34] were recorded with a polarimeter that used two telescopes and two Wollaston-prism analyzers to record simultaneous measurements of the signal in four polarization states, 0°, 45°, 90°, and 135°. We recorded polarization measurements with a division-of-focal-plane polarization camera, which recorded images of the Moon at polarization states of 0°, 45°, 90°, and 135° simultaneously. Images were recorded without a spectral filter [35] and through VNIR spectral filters [37], and pixels were averaged across the polarized images to calculate the disk-averaged DoLP. In both studies, all four polarization measurements were used to determine the normalized first and second Stokes parameters, s_1 and s_2, and the DoLP was calculated as $\text{DoLP} = (s_1^2 + s_2^2)^{1/2}$. The algebraic sign of the DoLP was added to represent whether the polarization state was perpendicular to the plane containing the Sun, the Moon, and the observer (positive sign) or parallel to this plane (negative sign).

Using this method, we recorded measurements of the disk-averaged DoLP in six channels: "broadband" [35] and five narrower bands centered at 450 nm (full-width at half-maximum bandwidth of 50, 520 (90), 650 (50), 800 (50), and 900 (50 nm) [38]). The broadband channel had a spectral response across the VNIR, from approximately 400 to 1000 nm. Coyne and Pellicori [34] recorded measurements of the disk-averaged DoLP in spectral bands centered at 336.0 nm (effective bandwidth of 33), 362.5 (36), 367.0 (44), 383.0 (25), 449.0 (110), 450.2 (49), 518.7 (92), and 534.0 (56 nm). Over the whole measurement period, the filters centered at 336.0 and 383.0 nm were always used; the filters centered at 367.0, 449.0, and 518.7 nm were used for their first measurement period and replaced by filters centered at 362.5, 450.2, and 534.0 nm, respectively. We chose to combine the data recorded with the 367.0- and 362.5-nm filters into one set of measurements, referred to by a wavelength of 365 nm. Similarly, we combined data recorded with the 449.0- and 450.2-nm filters as well as the measurements we recorded in a 450-nm band into one set of measurements, referred to by a wavelength of 450 nm. Finally, we combined Coyne and Pellicori's 518.7-nm data with the measurements we recorded in a 520-nm channel, referred to by a wavelength of 519 nm. We chose to exclude measurements with limited phase angles in the 534.0-nm channel and measurements obtained during a lunar eclipse. In summary, we fit a model for nine spectral channels: 336, 365, 383, 450, 519, 650, 800, 900 nm, and broadband. Fig. 1 summarizes how we combined the three datasets as well as which channels were fit to models with and without libration variables (see Section III-A).

Finally, we used the JPL Horizons tool [39] to calculate the absolute phase angle, Sun selenographic longitude, and observer selenographic latitude and longitude corresponding to the date of each observation. We found that the difference in measurement location for Coyne and Pellicori's dataset and our datasets made a negligible change in the calculated lunar geometry variables, so we performed all calculations with one measurement location (Bozeman, MT, USA). The DoLP measurements in the nine spectral channels are shown as a function of signed phase angle in Fig. 2.

III. Lunar Polarization Model

Our objective for LAMP was to predict the disk-averaged DoLP from the lunar geometry for the spectral bands where data were recorded. Thus, we used lunar geometry terms as independent variables in the model. Ultimately, this could enable predictions of the DoLP observed at the geometry of an on-orbit polarization-sensitive satellite and increase the accuracy of its lunar calibration. Following a similar approach

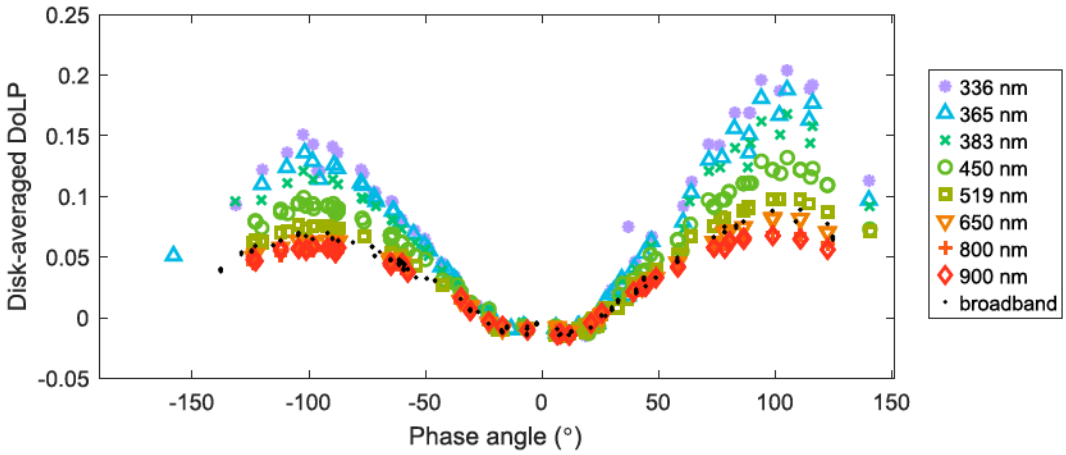


Fig. 2. Disk-averaged DoLP measurements for the nine spectral channels that were modeled.

to Kieffer and Stone's lunar irradiance model (the ROLO model) [20], we considered including the absolute phase angle, Sun selenographic longitude, and the observer selenographic latitude and longitude as independent variables in the model. The absolute phase angle was directly related to the angle at which sunlight was scattered and reflected by the lunar surface toward the observer, so the polarization state of observed moonlight depended strongly on the absolute phase angle. The Sun selenographic longitude controlled which part of the lunar surface was illuminated. Different regions of the lunar surface had different properties (such as lunar regolith particle size), so the polarization of moonlight varied with lunar region. Thus, we accounted for the effect on the disk-averaged polarization by using the Sun selenographic longitude as an independent variable. The observer selenographic latitude and longitude (referred to as "libration") controlled which part of the Moon was seen by the observer, similarly affecting the disk-averaged polarization. However, the libration/lunar phase cycle was 18 years, so we only used the libration variables when we had sufficient sampling of the possible libration values (see Section III-A).

Since DoLP and albedo are inversely correlated (Umov's effect [40]), it made sense for a model of DoLP to use similar polynomials of independent variables as the ROLO model of albedo. The ROLO model had absolute phase angle terms up to the third power and odd Sun selenographic longitude terms up to the fifth power, with different coefficients for each spectral band. It also had first-power interaction terms between the libration variables and Sun selenographic longitude, with one set of coefficients applied to all spectral bands. There were also exponential terms to describe the opposition effect, a sharp increase in brightness at small phase angles. While there is an increase in DoLP at small phase angles, it is small and can be modeled without exponential terms.

We allowed absolute phase angle terms up to the fourth power because this was above the minimum needed to capture the two inflection points present in the polarization curve (Fig. 2). Since this was an empirical model, the primary risk in including terms above the minimum needed was overfitting, but there were enough observations to include the fourth-power term.

We initially allowed all Sun selenographic longitude terms up to the fifth power, found that the second and fourth power terms were generally negligible, and followed the ROLO model in excluding them. Also, there was the following physical reasoning to exclude the even terms: the signed phase angle and the Sun selenographic longitude were geometrically related and thus highly correlated, but we used the absolute phase angle, so it had a similar magnitude to the Sun selenographic longitude but not always the same sign. Thus, the even power terms of absolute phase angle and Sun selenographic longitude were highly correlated, and removing the second and fourth power Sun selenographic longitude terms potentially helped us avoid problems from multicollinearity. Conceptually, the absolute phase angle terms created the shape of the curve that was symmetric for waxing and waning phases (i.e., the positive and negative signed phase angles), and the Sun selenographic latitude terms accounted for the asymmetry between the waxing and waning phases. The second- and fourth-power terms for Sun selenographic latitude had the same value regardless of the sign of the Sun selenographic latitude, so they did not create any differences between the waxing and waning phases. In other words, the second- and fourth-power absolute phase angle terms could produce any effect that the second- and fourth-power Sun selenographic longitude terms could. Thus, we decided to use only the odd terms like the ROLO model.

Finally, we included libration terms and interactions with Sun selenographic libration for some spectral channels as described in Section III-A. When the libration terms were included, only the first-power terms were used. If more observations are available in the future, it could be possible that including higher-order terms in an empirical model would provide some benefit, but we believed it was best to use only first-power terms with the current dataset.

The form of the model when the libration terms were not used was

$$\begin{aligned}\text{DoLP} = {} & a_1 g^4 + a_2 g^3 + a_3 g^2 + a_4 g \\ & + b_1 \Phi^5 + b_2 \Phi^3 + b_3 \Phi + c \end{aligned} \tag{1}$$

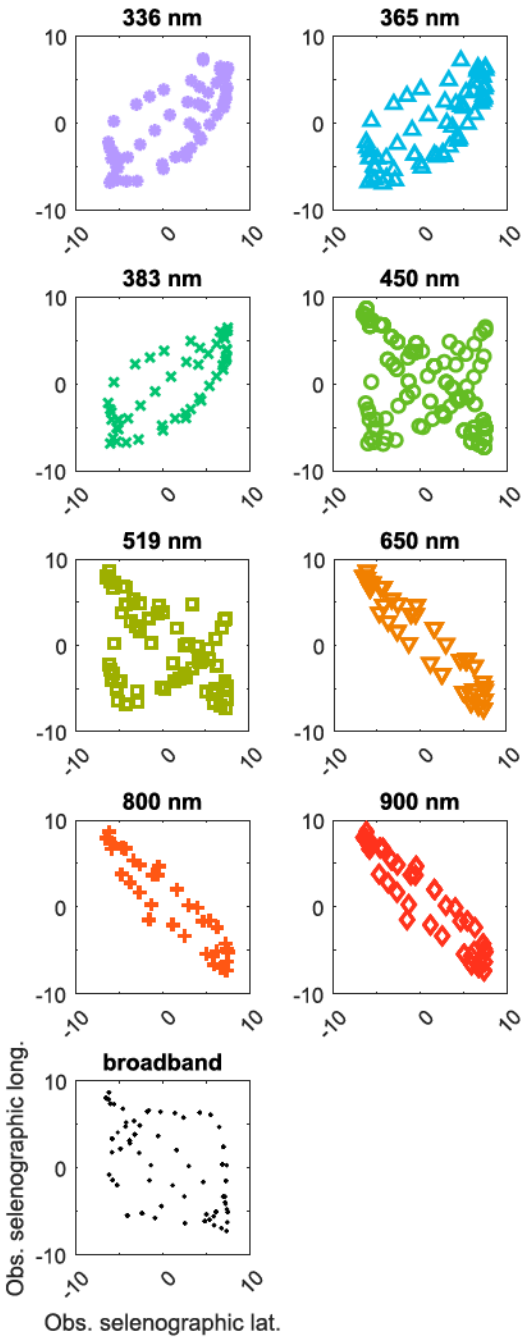


Fig. 3. Sampling of libration space for the nine spectral channels that were modeled. Each point shows the observer selenographic latitude and longitude where a measurement was recorded.

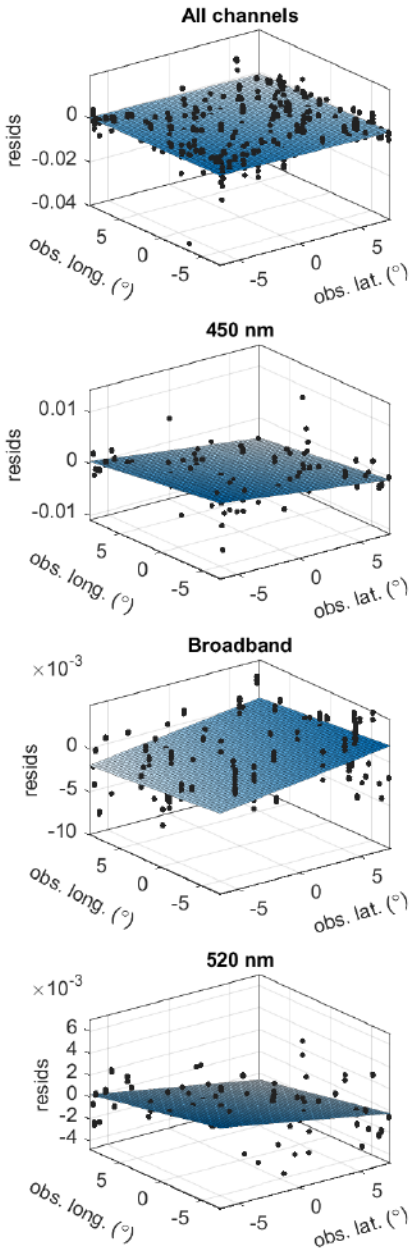


Fig. 4. Residuals after fitting to (1), shown with a best-fit plane. The residuals had little dependence on observer selenographic latitude and longitude when all channels were considered together, but a stronger dependence when the 450-nm, 519-nm, and broadband channels were considered individually.

where g was the absolute phase angle and Φ was the Sun selenographic longitude. The form of the model, including libration terms, was

$$\begin{aligned}\text{DoLP} = {} & a_1 g^4 + a_2 g^3 + a_3 g^2 + a_4 g \\ & + b_1 \Phi^5 + b_2 \Phi^3 + b_3 \Phi + c_1 \theta + c_2 \phi \\ & + d_1 \theta \Phi + d_2 \phi \Phi + e \end{aligned} \tag{2}$$

where g was the absolute phase angle, Φ was the Sun selenographic longitude, θ was the observer selenographic latitude, and ϕ was the observer selenographic longitude.

A. Libration Usage

To determine whether and how to include libration terms in the model for each spectral channel, we first investigated the sampling of the libration space. We plotted the observer selenographic latitude and longitude of all observations, shown in Fig. 3. The plot showed that the 450-nm, 519-nm, and broadband channels had moderate sampling across the libration space, but the other six spectral channels did not. Thus, the libration terms could not be used for these six spectral channels individually.

However, we considered whether it was possible to use one set of coefficients for the libration terms for all spectral

TABLE I
MODIFIED COEFFICIENTS CORRESPONDING TO (3) FOR THE MODELS WITHOUT LIBRATION VARIABLES FOR ALL NINE CHANNELS

Coefficient	336 nm	365 nm	383 nm	450 nm	519 nm	650 nm	800 nm	900 nm	broadband
a'_1	1.1989	8.4664	10.952	9.6088	13.239	9.3045	11.060	9.2387	10.380
a'_2	−3.6683	−5.2831	−5.6712	−4.6601	−5.0789	−3.9033	−3.9604	−3.4070	−4.4411
a'_3	5.6242	6.8038	6.8692	5.3827	5.2345	4.1384	3.7637	3.1347	4.8588
a'_4	−2.8837	−7.8868	−8.6177	−5.0548	−5.0611	−3.4020	−1.5472	1.3255	−6.0330
b'_1	1.8610	2.6377	2.3512	1.4425	0.70004	1.2704	0.63014	0.71832	0.68355
b'_2	−4.5324	−5.6974	−5.2002	−3.2085	−1.6708	−2.6193	−1.3188	−1.2907	−1.2548
b'_3	−1.0859	7.4533	7.3101	2.3292	−1.7735	3.1473	−0.80328	0.38393	−2.7667
c'	−1.4209	−0.88819	−0.83303	−1.04260	−1.1686	−1.0286	−1.3008	−1.6289	−0.87868

channels as in the ROLO model [20] with the following steps. First, we fit all channels individually with libration terms with (2). Second, the nine sets of coefficients c_1, c_2, d_1, and d_2 were averaged. Third, the models were refit again using the form of (2) but using the average values for c_1, c_2, d_1, and d_2 to find the optimal values of a_1–a_4, b_1–b_3, and e separately for each channel. The mean absolute residuals were the same or higher using this approach compared to not accounting for libration at all, using (1) separately for each channel. This suggested that one set of libration coefficients did not adequately describe the behavior across all spectral channels. To further explore this behavior, we examined the residuals of the model without libration, fit to (1). Fig. 4 shows the residuals as a function of observer selenographic latitude and longitude for all nine channels combined as well as for the 450-nm, 519-nm, and broadband channels individually. The residuals were plotted with a best-fit plane to enable easier identification of trends. The residuals for all channels considered together (top left in Fig. 4) had a best-fit plane close to horizontal, indicating that the DoLP did not depend on observer selenographic latitude and longitude across all channels. This explained why using the libration coefficients averaged across all channels showed no improvement. This conclusion was further supported by the residuals depending on the libration variables in different ways in the 450-nm, 519-nm, and broadband channels (e.g., the residuals tended to be positive for negative observer selenographic latitudes for the 450-nm channel, but the broadband channels had negative residuals for negative observer selenographic latitudes).

Based on these findings, we made the following conclusion about how to include libration variables in the model: 1) one set of libration coefficients could not be used across all nine channels and 2) only some channels had enough sampling of the libration space to use (2) fit individually for the channel. Thus, we created fits to (1) without libration for all nine channels, but we only created additional fits to (2) with libration for the 450-nm, 519-nm, and broadband channels. A graphical summary outlining which models were created for the nine spectral channels and their data source is shown in Fig. 1.

B. Models Without Libration

This section presents the models without libration variables; the fits for all nine channels are provided. To avoid including the order of magnitude of the coefficients repeatedly in Table I, we explicitly separated the order of magnitude from the coefficients and rewrote (1) as

$$\begin{aligned}\text{DoLP} = &\left(a'_1 \cdot 10^{-10}\right)\ g^4 + \left(a'_2 \cdot 10^{-7}\right)\ g^3 \\ &+ \left(a'_3 \cdot 10^{-5}\right)\ g^2 + \left(a'_4 \cdot 10^{-4}\right)\ g \\ &+ \left(b'_1 \cdot 10^{-12}\right)\ \Phi^5 + \left(b'_2 \cdot 10^{-8}\right)\ \Phi^3 \\ &+ \left(b'_3 \cdot 10^{-5}\right)\ \Phi + \left(c' \cdot 10^{-2}\right). \end{aligned} \tag{3}$$

Thus, (3) is the same as (1), and the values of the modified coefficients are shown in Table I.

As examples, the measured and fit data are shown together along with plots of the residuals for the 383-nm channel in Fig. 5 and for the 650-nm channel in Fig. 6. For both channels shown and for the other channels not shown, two important assumptions for using a generalized linear model were satisfied: the residuals were approximately normally distributed, and they did not show a strong trend with fit DoLP.

For the 383-nm band, the mean absolute residual was 0.0043, and all residuals were between −0.013 and 0.020. It appeared that a major contribution to the residuals was not accounting for libration. For the predicted values in the phase angle range of 60°–116° (which appeared to fall farthest from the measured values), almost all negative residuals corresponded to a positive observer selenographic latitude, and almost all positive residuals corresponded to a negative observer selenographic latitude. This was explained by the Moon's asymmetry across the equator (when more lunar surface areas with low albedo and high polarization were illuminated and visible to the observer, the disk-averaged DoLP was higher).

For the 650-nm channel, the mean absolute residual was 0.0010, and all residuals were between −0.0036 and 0.0040. The agreement between the measured and predicted DoLP in Fig. 6 was closer than that for 383 nm, but the most likely cause was again libration. Because the 650-nm dataset was recorded over approximately one year and fewer lunations than the 383-nm dataset, all observations with a phase angle greater than 50° had a negative value of observer selenographic latitude. Thus, even though libration variables were not included in the model, the fit for 650 nm was optimized for negative values of observer selenographic latitude. If the 650-nm dataset spanned more lunations, the residuals would likely have been larger. Another reason that the residuals were smaller for 650 nm than for 383 nm was that the DoLP had a lower magnitude for 650 nm than for 383 nm (e.g., the observed maximum for waning phases was 0.168 for the 383-nm channel and 0.0822 for the 650-nm channel).

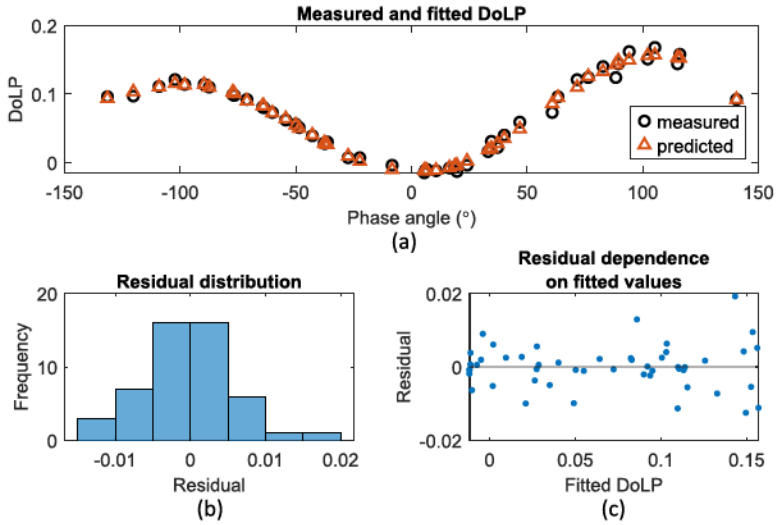


Fig. 5. Model without libration variables fit to (1) for the 383-nm channel with (a) measured and predicted DoLP values, (b) distribution of the residuals, and (c) dependence of the residuals on fit DoLP shown.

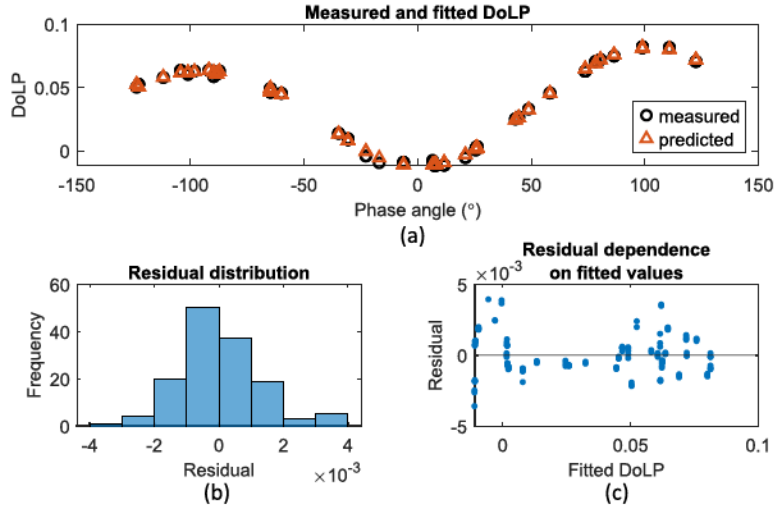


Fig. 6. Model without libration variables fit to (1) for the 650-nm channel with (a) measured and predicted DoLP values, (b) distribution of the residuals, and (c) dependence of the residuals on fit DoLP shown.

TABLE II
MEAN AND MAXIMUM RESIDUALS FOR THE MODELS WITHOUT LIBRATION VARIABLES

Channel	$mean\|resid\|$	$max\|resid\|$	Measured DoLP range
336 nm	0.0056	0.038	-0.015 to 0.204
365 nm	0.0046	0.022	-0.013 to 0.188
383 nm	0.0043	0.019	-0.015 to 0.168
450 nm	0.0021	0.014	-0.014 to 0.132
519 nm	0.0014	0.0070	-0.016 to 0.098
650 nm	0.0010	0.0039	-0.012 to 0.082
800 nm	0.00087	0.0026	-0.012 to 0.070
900 nm	0.0015	0.0043	-0.015 to 0.068
broadband	0.0024	0.0073	-0.014 to 0.089

The trends observed for the 383- and 650-nm channels were consistent through the rest of the channels not shown. The channels with datasets spanning more lunations tended to have higher residuals and an apparent relationship between the sign of the residuals and the sign of the libration variables. On the other hand, the channels with datasets spanning fewer lunations tended to have lower residuals, but it is likely that the residuals would increase if more data were recorded at different librations. In addition, residuals generally decreased with wavelength, but the channels with the longest wavelengths had datasets that spanned fewer lunations, so these effects were not independent. The mean and maximum absolute residuals are included in Table II. The range of measured DoLP values in each channel was also included in Table II to provide context for the magnitude of the residuals.

C. Models With Libration

For the channels with moderate sampling of the libration space (450 nm, 519 nm, and broadband), a second model was fit to (2) with libration variables. As with the models without libration, to avoid writing the order of magnitude of coefficients repeatedly, the coefficients were modified according

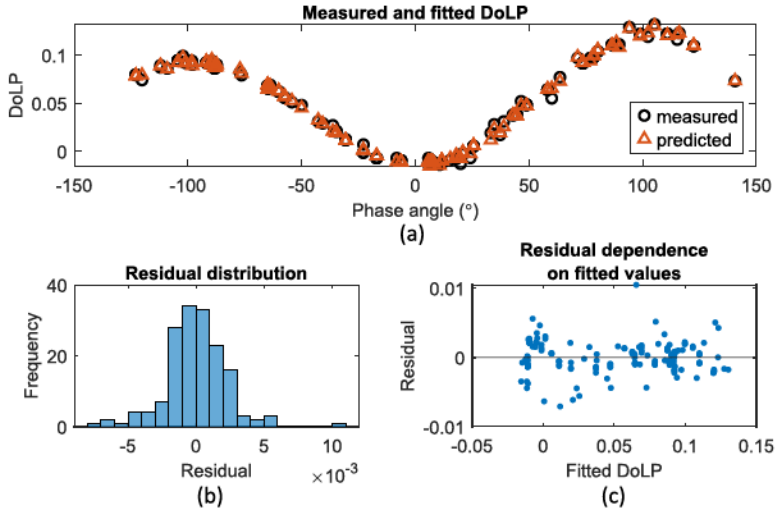


Fig. 7. Model with libration variables fit to (2) for the 450-nm channel with (a) measured and predicted DoLP values, (b) distribution of the residuals, and (c) dependence of the residuals on fit DoLP shown.

TABLE III
MODIFIED COEFFICIENTS CORRESPONDING TO (4) FOR THE MODELS WITH LIBRATION VARIABLES FOR THE 450-NM, 519-NM, AND BROADBAND CHANNELS

Coefficient	450 nm	519 nm	broadband
a'_1	1.0165	1.3362	1.0207
a'_2	−4.8169	−5.1745	−4.3082
a'_3	5.5038	5.3708	4.6710
a'_4	−5.2069	−5.5156	−5.3352
b'_1	18.503	8.4055	6.6049
b'_2	−3.7386	−1.8795	−1.3161
b'_3	3.5234	−1.8541	−1.5805
c'_1	3.0301	2.5576	−1.4996
c'_2	1.6673	1.2406	1.4851
d'_1	−6.7661	−1.9864	−0.24788
d'_2	−5.5464	−0.92855	−2.5665
e'	−1.1156	−1.1779	−0.91466

to (4), and the modified coefficients are included in Table III

$$\begin{aligned}\text{DoLP} = &\left(a'_1 \cdot 10^{-9}\right)\, g^4 + \left(a'_2 \cdot 10^{-7}\right)\, g^3 \\ &+ \left(a'_3 \cdot 10^{-5}\right)\, g^2 + \left(a'_4 \cdot 10^{-4}\right)\, g \\ &+ \left(b'_1 \cdot 10^{-13}\right)\, \Phi^5 + \left(b'_2 \cdot 10^{-8}\right)\, \Phi^3 \\ &+ \left(b'_3 \cdot 10^{-5}\right)\, \Phi \\ &+ \left(c'_1 \cdot 10^{-4}\right)\, \theta + \left(c'_2 \cdot 10^{-4}\right)\, \phi \\ &+ \left(d'_1 \cdot 10^{-6}\right)\, \theta\Phi + \left(d'_2 \cdot 10^{-6}\right)\, \phi\Phi + \left(e' \cdot 10^{-2}\right). \end{aligned} \tag{4}$$

Thus, (4) is the same as (2).

The measured and modeled data for the 450-nm channel are shown in Fig. 7. The measured and predicted DoLP values qualitatively appeared to match well, and the predictions matched the rapidly varying shape of the measured data near a phase angle of 100° better than the model without libration. The mean absolute residual was 0.0017, and all residuals were between −0.0071 and 0.011. For the 519-nm fit, the mean absolute residual was 0.0013, and all residuals were between −0.0053 and 0.0041. For the broadband fit, the mean absolute residual was 0.0021, and all residuals were between −0.0060 and 0.0048. All three fits with libration had smaller residuals than the corresponding fits without libration.

As a secondary confirmation that the model was fitting to a libration effect and not noise, we fit the same model but with a subset of the data that only included measurements outside the rapidly varying region of 85°–116°. We fit the new model and used it to predict the DoLP for all observations (including 85°–116°). The mean absolute residual was 0.0017 and all residuals were between −0.0072 and 0.011. Fig. 8 shows the measured and predicted DoLP values together as well as the residuals. Even though some data were excluded in fitting the model, the residuals were extremely similar to the model using the whole dataset, and the qualitative agreement between the measured and predicted values in the range of 85°–116° did not appear to decrease. In addition to this confirmation, we noticed the same pattern that was described for the 383-nm channel: the measurements and predictions that had a higher DoLP in the range from 85° to 116° tended to correspond to observations with positive observer selenographic latitudes.

D. Example Predictions

As an example, we used LAMP to predict the disk-averaged DoLP at six phase angles and zero libration for all channels except broadband and plotted them as a function of wavelength in Fig. 9. For 450 and 519 nm, we used the fits that included libration variables. Even though the libration variables were set to zero, the other coefficients were slightly different for the fits with and without libration, so this was not the same as using the fits without libration variables.

As expected, the predictions showed the same trends that were identified in the previously published datasets [34], [37]. The DoLP decreased with wavelength, with the exception of the 900-nm channel, which had a higher DoLP than the 800-nm channel for waxing phases. The DoLP was negative for a phase angle of 15° and positive for phase angles 30° and greater. The phase angle of maximum DoLP also appeared to decrease as the wavelength increased. This was seen most

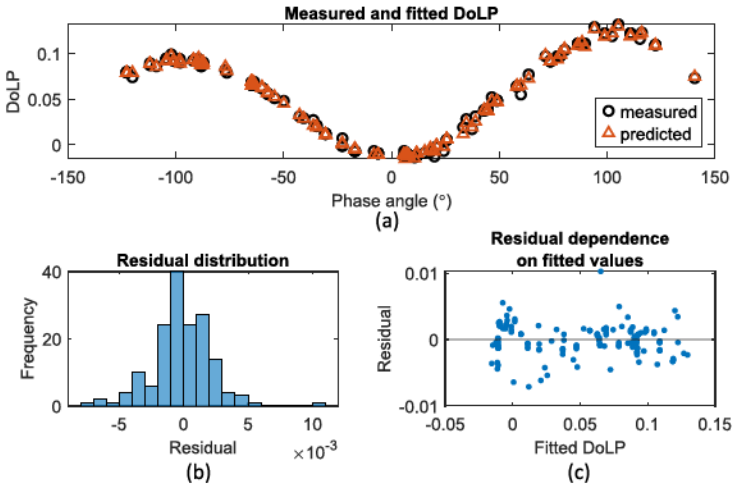


Fig. 8. Model with libration variables fit to (2) for the 450-nm channel fit with a subset of the data excluding 85° to 116° with (a) measured and predicted DoLP values, (b) distribution of the residuals, and (c) dependence of the residuals on fit DoLP shown.

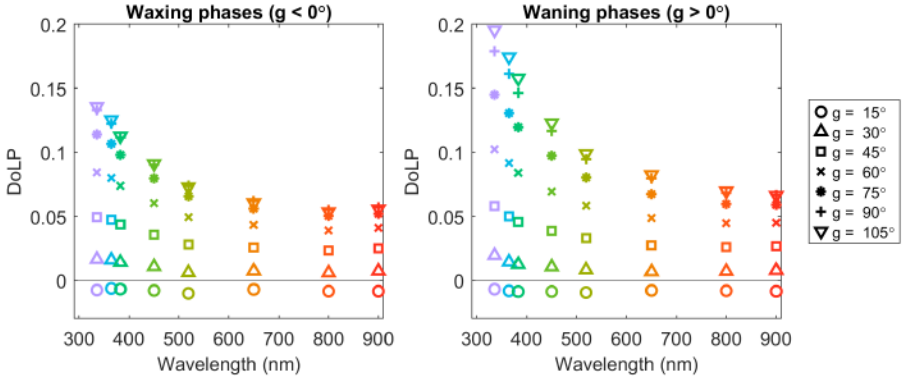


Fig. 9. Predicted disk-averaged DoLP for (left) waxing and (right) waning phases. DoLP was predicted for phase angles (g) ranging from 15° to 105° in 15°-steps and zero libration.

clearly for waning phases, as the predicted DoLP was higher for 105° than 90° for the UV channels, but predicted values grew closer together as the wavelength increased.

Using predictions like the ones in Fig. 9, we could use the model results to predict the disk-averaged DoLP that would be observed by an arbitrary instrument operating between 336 and 900 nm. This could be achieved by predicting the DoLP as a function of wavelength for the relevant lunar geometry and then interpolating to estimate the DoLP in the spectral band of the instrument.

E. Estimating the Inversion Angle

We also used the model to estimate the inversion angle at which the polarization flips from negative to positive, which could be useful for identifying when an on-orbit instrument could use the disk average of the Moon as an unpolarized calibration target. We predicted DoLP values for phase angles from 19° to 25° in 0.1° steps and zero libration, and the phase angle at which the DoLP had a minimum absolute value was reported as the inversion angle. The results are summarized in Fig. 10.

The inversion angle generally increased with wavelength, which has been reported previously [41]. However, the

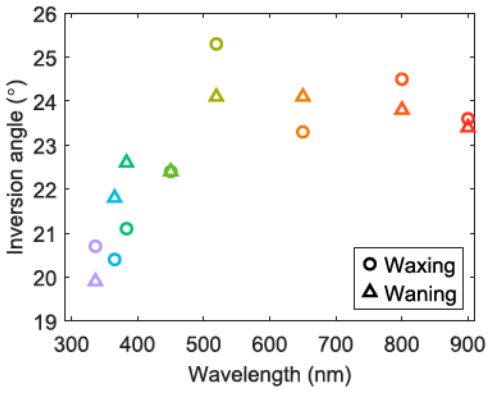


Fig. 10. Inversion angle estimated with the model, assuming zero libration.

specific value of the inversion angle appeared to change considerably with the values of the libration variable. For example, at an absolute phase angle of 20.9°, Sun selenographic longitude of −20.6°, observer selenographic latitude of 3.0°, and observer selenographic longitude of 0.2°, the predicted DoLP in the 450-nm channel was −0.0012. However, at a higher absolute phase angle of 24.2°, Sun selenographic longitude of −26.8°, observer selenographic latitude of −5.8°,

and observer selenographic longitude of −4.1°, the predicted DoLP in the 450-nm channel was −0.0024. Assuming similar rates of increase of DoLP for both cases, this suggested that the inversion angle could change by approximately 3° depending on the libration values. The values in Fig. 10 were within 3° of estimates of the inversion angle previously made by Dollfus and Bowell [41] (but there is ambiguity in the lunar region(s) described by their measurements).

F. Prediction Accuracy

The accuracy with which this model can be used to predict the disk-averaged DoLP depends on several factors. First, the uncertainty of the measured data, especially systematic errors, would affect the resulting model. Second, the extent to which the empirical model captured the true variation of moonlight polarization also affects the overall accuracy. For instance, there was likely a very small dependence on Sun selenographic latitude that was ignored. Similarly, the limited sampling of the libration/lunar phase cycle decreased the accuracy of the model. Particularly for the 650-, 800-, and 900-nm channels, the fits represented the closest match to the data for only a small range of the possible values of the libration variables and therefore would not fit as well to data recorded at other values of the libration variables. Finally, when using the model to predict the DoLP observed by a certain instrument at a certain geometry, unless the instrument has the same spectral response as one of the nine channels used in this work, there would be some uncertainty resulting from interpolating to a different wavelength and/or bandwidth. While we did not attempt to combine the effects of the known uncertainties in this list (and could not include the unknown uncertainties), the residuals were generally larger than the reported measurement uncertainties [34], [35], [37]. We believe that the residuals for the channels without small libration coverage provide a reasonable assessment of the model performance: the residuals for the models without libration variables were generally less than 0.01 and the residuals for the models with libration variables were generally less than 0.005.

G. Comparison to LIME

We compared the DoLP predicted by our models without libration to a prediction by the preliminary DoLP model of LIME. Both models were used to predict DoLP at a phase angle of −90°, and we found that the difference in DoLP predicted by LIME and LAMP was always less than 0.01. The DoLP predicted by LIME was 8.7% lower than the DoLP we predicted at 450 nm, 5.0% lower at 519 nm, 6.6% lower at 650 nm, 13.8% higher at 800 nm, and 15.5% higher at 900 nm. Thus, the difference between the models was similar in magnitude to the residuals of the models without libration, and it is possible that the agreement will improve as this preliminary DoLP model from LIME is finalized.

IV. Conclusion

The set of Moon polarization models presented in this work, collectively called LAMP, can be used to predict the disk-averaged DoLP with the lunar geometry in eight spectral channels ranging from 336 to 900 nm as well as in a VNIR broadband channel. The models followed the approach used by Kieffer and Stone's lunar irradiance model [20]. For the 450-nm, 519-nm, and broadband channels, the predicted DoLP depended on the value of the libration variables (observer selenographic latitude and longitude), but the rest of the models did not. We used the models to predict the disk-averaged DoLP at a set of illustrative phase angles as well as phase angles between 19° and 25° to estimate the inversion angle. The residuals for the models with libration were generally within 0.005, and the residuals for the models without libration were generally within 0.01 (with a DoLP scale from 0 to 1). A longer set of observations spanning more of the libration/lunar phase cycle is necessary to develop models with libration for all channels modeled in this work, which would be an important step toward increasing the accuracy of this (or any) model of Moon polarization.

While the DoLP can only be predicted directly at eight spectral channels, the predicted DoLP values varied smoothly with wavelength, so interpolation can enable predicting the DoLP in an arbitrary spectral band between 336 and 900 nm. This could be useful for increasing the accuracy of lunar calibration of polarization-sensitive satellite instruments. It could also be possible to use the model to estimate when a satellite instrument would have a lunar-view opportunity close to the inversion angle and perform lunar calibration with a very low DoLP. With the recent and planned launches of polarimeters [42], [43], the improved lunar calibration accuracy enabled by these Moon polarization models could ultimately impact an increasing amount of polarimetric environmental remote sensing data.

Acknowledgment

Any opinions, findings, and conclusion or recommendation expressed in this article are those of the authors and do not necessarily reflect the views of the National Science Foundation.

References

[1] B. R. Barkstrom, "The Earth radiation budget experiment (ERBE)," *Bull. Amer. Meteorological Soc.*, vol. 65, no. 11, pp. 1170–1185, Nov. 1984.
[2] N. G. Loeb, D. R. Doelling, S. Kato, W. Su, P. E. Mlynczak, and J. C. Wilkins, "Continuity in top-of-atmosphere Earth radiation budget observations," *J. Climate*, vol. 37, no. 23, pp. 6093–6108, Dec. 2024.
[3] Q. Mu, F. A. Heinsch, M. Zhao, and S. W. Running, "Development of a global evapotranspiration algorithm based on MODIS and global meteorology data," *Remote Sens. Environ.*, vol. 111, no. 4, pp. 519–536, Dec. 2007.
[4] S. I. Hay, R. W. Snow, and D. J. Rogers, "Predicting malaria seasons in Kenya using multitemporal Meteorological Satellite sensor data," *Trans. Roy. Soc. Tropical Med. Hygiene*, vol. 92, no. 1, pp. 12–20, Jan. 1998.
[5] G. Chander, T. J. Hewison, N. Fox, X. Wu, X. Xiong, and W. J. Blackwell, "Overview of intercalibration of satellite instruments," *IEEE Trans. Geosci. Remote Sens.*, vol. 51, no. 3, pp. 1056–1080, Mar. 2013.
[6] A. C. Povey and R. G. Grainger, "Known and unknown unknowns: Uncertainty estimation in satellite remote sensing," *Atmos. Meas. Techn.*, vol. 8, no. 11, pp. 4699–4718, Nov. 2015.
[7] R. B. Lee, L. M. Avis, M. A. Gibson, and L. P. Kopia, "Characterizations of the mirror attenuator mosaic: Solar diffuser plate," *Appl. Opt.*, vol. 31, no. 31, pp. 6643–6652, 1992.
[8] R. E. Eplee Jr., F. S. Patt, R. A. Barnes, and C. R. McClain, "SeaWiFS long-term solar diffuser reflectance and sensor noise analyses," *Appl. Opt.*, vol. 46, no. 5, pp. 762–773, 2007.
[9] X. Xiong, A. Angal, J. Sun, T. Choi, and E. Johnson, "On-orbit performance of MODIS solar diffuser stability monitor," *J. Appl. Remote Sens.*, vol. 8, no. 1, Nov. 2014, Art. no. 083514.

[10] J. Sun and M. Wang, "On-orbit calibration of Visible Infrared Imaging Radiometer Suite reflective solar bands and its challenges using a solar diffuser," *Appl. Opt.*, vol. 54, no. 24, pp. 7210–7223, 2015.
[11] J. McIntire, S. Lee, R. E. Eplee, and G. Meister, "PACE OCI on-orbit solar calibration," *Proc. SPIE*, vol. 13143, p. 24, Oct. 2024, Art. no. 131430M.
[12] B. L. Markham et al., "Landsat-7 ETM+ on-orbit reflective-band radiometric stability and absolute calibration," *IEEE Trans. Geosci. Remote Sens.*, vol. 42, no. 12, pp. 2810–2820, Dec. 2004.
[13] X. Xiong, B. N. Wenny, A. Wu, and W. L. Barnes, "MODIS onboard blackbody function and performance," *IEEE Trans. Geosci. Remote Sens.*, vol. 47, no. 12, pp. 4210–4222, Dec. 2009.
[14] D. Helder et al., "Absolute radiometric calibration of Landsat using a pseudo invariant calibration site," *IEEE Trans. Geosci. Remote Sens.*, vol. 51, no. 3, pp. 1360–1369, Mar. 2013.
[15] M. Bouvet et al., "RadCalNet: A radiometric calibration network for Earth observing imagers operating in the visible to shortwave infrared spectral range," *Remote Sens.*, vol. 11, no. 20, p. 2401, Oct. 2019.
[16] K. G. Ruddick et al., "HYPERNETS: A network of automated hyperspectral radiometers to validate water and land surface reflectance (380–1680 nm) from all satellite missions," *Frontiers Remote Sens.*, vol. 5, Apr. 2024, Art. no. 1372085.
[17] G. Zibordi et al., "Advances in the ocean color component of the aerosol robotic network (AERONET-OC)," *J. Atmos. Ocean. Technol.*, vol. 38, no. 4, pp. 725–746, Apr. 2021.
[18] D. R. Doelling, D. Morstad, B. R. Scarino, R. Bhatt, and A. Gopalan, "The characterization of deep convective clouds as an invariant calibration target and as a visible calibration technique," *IEEE Trans. Geosci. Remote Sens.*, vol. 51, no. 3, pp. 1147–1159, Mar. 2013.
[19] N. Fox and P. Green, "Traceable radiometry underpinning Terrestrial- and helio-studies (TRUTHS): An element of a space-based climate and calibration observatory," *Remote Sens.*, vol. 12, no. 15, p. 2400, Jul. 2020.
[20] H. H. Kieffer and T. C. Stone, "The spectral irradiance of the moon," *Astronomical J.*, vol. 129, no. 6, pp. 2887–2901, Jun. 2005.
[21] Y. Shea et al., "Clarreo pathfinder: Mission overview and current status," in *Proc. IEEE Int. Geosci. Remote Sens. Symp. (IGARSS)*, Waikoloa, HI, USA, Sep. 2020, pp. 3286–3289.
[22] J. T. Woodward et al., "Measurements of absolute, SI-traceable lunar irradiance with the airborne lunar spectral irradiance (air-LUSI) instrument," *Metrologia*, vol. 59, no. 3, Jun. 2022, Art. no. 034001.
[23] H. Courrier et al., "ARCSTONE: Calibration of lunar spectral reflectance from space. Prototype instrument concept, analysis, and results," *J. Appl. Remote Sens.*, vol. 17, no. 4, Nov. 2023, Art. no. 044508.
[24] C. Toledano et al., "LIME: Lunar irradiance model of ESA, a new tool for absolute radiometric calibration using the moon," *Atmos. Chem. Phys.*, vol. 24, no. 6, pp. 3649–3671, Mar. 2024.
[25] J.-Q. Sun and X. Xiong, "MODIS polarization-sensitivity analysis," *IEEE Trans. Geosci. Remote Sens.*, vol. 45, no. 9, pp. 2875–2885, Sep. 2007.
[26] R. E. Eplee et al., "On-orbit calibration of SeaWiFS," *Appl. Opt.*, vol. 51, no. 36, pp. 8702–8730, 2012.
[27] X. Xiong, J. Sun, J. Fulbright, Z. Wang, and J. J. Butler, "Lunar calibration and performance for S-NPP VIIRS reflective solar bands," *IEEE Trans. Geosci. Remote Sens.*, vol. 54, no. 2, pp. 1052–1061, Feb. 2016.
[28] J. L. Daniels, G. L. Smith, K. J. Priestley, and S. Thomas, "Using lunar observations to validate in-flight calibrations of Clouds and the Earth's Radiant Energy System instruments," *IEEE Trans. Geosci. Remote Sens.*, vol. 53, no. 9, pp. 5110–5116, Sep. 2015.
[29] D. Crisp et al., "The on-orbit performance of the Orbiting Carbon Observatory-2 (OCO-2) instrument and its radiometrically calibrated products," *Atmos. Meas. Techn.*, vol. 10, no. 1, pp. 59–81, Jan. 2017.
[30] S. Lee, F. Pratt, R. E. Eplee, J. McIntire, and G. Meister, "PACE OCI lunar calibration: Initial results," *Proc. SPIE*, vol. 13143, pp. 183–193, Oct. 2024.
[31] X. Xiong, J. Sun, A. Angal, and T. Wilson, "Calibration intercomparison of MODIS and VIIRS reflective solar bands using lunar observations," *Remote Sens.*, vol. 14, no. 19, p. 4754, Sep. 2022.
[32] T. C. Stone, H. Kieffer, C. Lukashin, and K. Turpie, "The moon as a climate-quality radiometric calibration reference," *Remote Sens.*, vol. 12, no. 11, p. 1837, Jun. 2020.
[33] E. Venkatesulu, E. C. Duley, and J. A. Shaw, "Polarization of the moon as a function of lunar phase angle in visible and near infrared spectral bands," *Proc. SPIE*, vol. 13615, Sep. 2025, Art. no. 136150J.
[34] G. V. Coyne and S. F. Pellicori, "Wavelength dependence of polarization. XX. The integrated disk of the moon," *Astronomical J.*, vol. 75, p. 54, Feb. 1970.
[35] E. Venkatesulu and J. A. Shaw, "Polarization images of the moon as a function of the lunar phase," *Opt. Exp.*, vol. 32, no. 14, pp. 24275–24292, 2024.
[36] E. Venkatesulu and J. Shaw, "Raw data, calibration files, and code for processing polarization images of the moon," Montana State Univ., Bozeman, MT, USA, Tech. Rep., Apr. 2024, doi: 10.6084/m9.figshare.25647987.v2.
[37] E. Venkatesulu, E. C. Duley, and J. A. Shaw, "Visible and near-infrared moon polarization across the lunar cycle," *J. Appl. Remote Sens.*, vol. 19, no. 4, Oct. 2025, Art. no. 044502.
[38] E. Venkatesulu, E. Duley, and J. Shaw, "Data, calibration data, and code for 'Visible and near infrared Moon polarization across the lunar cycle,'" Montana State Univ., Bozeman, MT, USA, Tech. Rep., May 2025, doi: 10.6084/m9.figshare.c.7835132.v2.
[39] Horizons web application. *Solar System Dynamics, Jet Propulsion Laboratory*. Accessed: Dec. 10, 2025. [Online]. Available: https://ssd.jpl.nasa.gov/horizons/app.html#/
[40] Y. Shkuratov, V. Kaydash, V. Korokhin, Y. Velikodsky, N. Opanasenko, and G. Videen, "Optical measurements of the moon as a tool to study its surface," *Planet. Space Sci.*, vol. 59, no. 13, pp. 1326–1371, Oct. 2011.
[41] A. Dollfus and E. Bowell, "Polarimetric properties of the lunar surface and its interpretation. Part I. Telescopic observations," *Astron. Astrophys.*, vol. 10, p. 29, Jan. 1971.
[42] P. J. Werdell et al., "Life after launch: A snapshot of the first six months of NASA's plankton, aerosol, cloud, ocean ecosystem (PACE) mission," *Proc. SPIE*, vol. 13192, pp. 70–84, Nov. 2024.
[43] S. A. Braun, J. Yorks, T. Thorsen, D. Cecil, and D. Kirschbaum, "NASA's Earth system observatory-atmosphere observing system," in *Proc. IEEE Int. Geosci. Remote Sens. Symp.*, Sep. 2022, pp. 7391–7393.



Erica Venkatesulu received the B.S. degree in electrical engineering from Pennsylvania State University, University Park, PA, USA, in 2020, and the M.S. degree in optics and photonics and the Ph.D. degree in electrical engineering from Montana State University, Bozeman, MT, USA, in 2022 and 2025, respectively.

She is a Research Engineer and an Assistant Teaching Professor with Montana State University. Her research interests include polarimetry and remote sensing.



Riley D. Logan (Member, IEEE) received the B.S. degree in electrical engineering, the M.S. degree in optics and photonics, and the Ph.D. degree in electrical engineering from Montana State University, Bozeman, MT, USA, in 2015, 2020, and 2024, respectively.

In 2025, he joined the Electrical and Computer Engineering Department, Montana State University, as an Assistant Professor. His research interests include environmental monitoring, spectral imaging, and biophotonics.



Joseph A. Shaw (Senior Member, IEEE) received the B.S. degree in electrical engineering from the University of Alaska Fairbanks, Fairbanks, AK, USA, in 1987, the M.S. degree in electrical engineering from the University of Utah, Salt Lake City, UT, USA, in 1989, and the M.S. and Ph.D. degrees in optical sciences from the University of Arizona, Tucson, AZ, USA, in 1994 and 1996, respectively.

He is the Director of the Optical Technology Center and a Distinguished Professor with the Norm Asbjornson College of Engineering, Montana State University, Bozeman, MT, USA, where he develops environmental remote sensing systems.

Dr. Shaw is a fellow of SPIE and Optica.